ACCEPTED VERSION

http://hdl.handle.net/2440/130610

A Summary of Experimental Studies on Heliostat Wind Loads in a Turbulent Atmospheric Boundary Layer

Maziar Arjomandi,[1, a)] Matthew Emes,[1, b)] Azadeh Jafari,[1, c)] Jeremy Yu,[1, d)] Farzin Ghanadi,[2, e)] Richard Kelso,[1, f)] Benjamin Cazzolato,[1, g)] Joe Coventry,[3, h)] Mike Collins[4, i)]

[1] *Centre for Energy Technology, School of Mechanical Engineering, University of Adelaide, Adelaide, SA 5005, Australia*
[2] *School of Engineering, University of Newcastle, Callaghan, NSW 2308, Australia.*
[3] *Research School of Electrical, Energy and Materials Engineering, Australian National University, Canberra, ACT 0200, Australia.*
[4]*CSIRO Energy, 10 Murray Dwyer Circuit, Mayfield West, NSW 2304, Australia.*

a) Corresponding author: maziar.arjomandi@adelaide.edu.au
b) matthew.emes@adelaide.edu.au
c) azadeh.jafari@adelaide.edu.au
d) jeremy.yu@adelaide.edu.au
e) farzin.ghanadi@newcastle.edu.au
f) richard.kelso@adelaide.edu.au
g) benjamin.cazzolato@adelaide.edu.au
h) joe.coventry@anu.edu.au
i) mike.collins@csiro.au

Abstract. The aerodynamic loads on heliostats have been investigated through an extensive range of experimental studies at the University of Adelaide in association with the Australian Solar Thermal Research Institute (ASTRI). Applied modelling techniques using spires and roughness elements were adopted for generation and characterisation of the temporal and spatial turbulence fluctuations, matching those in the lower region of the atmospheric boundary layer (ABL) where full-scale heliostats are positioned. Heliostat wind loads were found to be highly dependent on the critical scaling parameters of the heliostat and the turbulence intensities and scales in the ABL flow. The peak drag and lift coefficients on heliostats followed a similar variation with elevation and azimuth angles to those previously reported in the literature at a similar turbulence intensity. However, the current study revealed a linear increase of the peak drag and lift coefficients on heliostats in operating and stow positions with a parameter defined by the product of the turbulence intensity and the ratio of the turbulence length scales to the heliostat chord length.

INTRODUCTION

This article presents a comprehensive report on the aerodynamic wind loads on heliostats conducted by the University of Adelaide over the past six years, as part of the Australian Solar Thermal Research Institute (ASTRI). The experimental study significantly expands previous datasets produced in 1988-1992 by Peterka *et al.* [1, 2] through detailed characterization of turbulence intensities and length scales representing the atmospheric boundary layer (ABL) flow approaching heliostats at heights below 10 m in terrains ranging from a flat desert to a suburban area. Heliostat subcomponents influenced by wind loads – the elevation and azimuth drives, pedestal, foundation and mirror support structure – account for up to 80% of the capital cost of the heliostat field in a concentrating solar

thermal plant [3]. These costs can be most effectively reduced through improved estimation of the wind loading on a heliostat, leading to lower strength and stiffness requirements, hence the manufacture of lighter components that maintain their structural integrity during high wind periods while achieving good optical performance during operation of the field [4].

In the past six years, a series of experimental investigations [5-9] of the static and dynamic wind loads have been carried out using high-frequency force and surface pressure measurements on a range of heliostat sizes and azimuth-elevation configurations in the University of Adelaide wind tunnel. The results have been used to predict the design loads based on the critical scaling parameters of the heliostat and the surrounding terrain of a heliostat field site. This complements the maximum loading cases reported by Peterka and Derickson [1] that are commonly used for heliostat design based on a simulated ABL over an "open country" terrain at a turbulence intensity $I_u = 18\%$. The data in the current study forms part of "Heliostat wind load guidelines" that can be used to design any heliostat structure. The load distributions and aerodynamic coefficients have formed part of the structural design of the tilt-roll CSIRO heliostat and assisted in the design of the drive units, pedestal and foundation in a conventional elevation-azimuth heliostat.

METHODOLOGY

Experimental measurements were taken in a closed-return wind tunnel at the University of Adelaide. Figure 1 shows a schematic diagram of the tunnel with the setup used for generation of the ABL, instrumentation used for characterization of the turbulent flow characteristics and measurement of the loads on scale-model heliostats. The test section of the tunnel has a development length of 17 m and a cross-section expanding to 3 m $\times$ 3 m to allow for a pressure gradient resulting from growth of the boundary layer. Following the empirical method of Irwin [10], truncated wooden spires of various heights and base widths [5, 7, 8] were used to simulate the lower region of the ABL and roughness elements were placed in a staggered arrangement over a fetch of 10 m with spacing of 0.5 m in the longitudinal x and lateral y directions. The spires, ranging from heights of 1.3 m to 2 m and base widths of 0.155 m to 0.56 m, produced boundary layer velocity and turbulence profiles characterised in the lowest 100 m of terrain ranging from a flat desert to a suburban area [8]. Three components of velocity were sampled at 1 kHz at different heights and spanwise positions using a Turbulent Flow Instrumentation Cobra probe and a two-dimensional traverse (Figure 2c). The wind tunnel freestream velocity $U_\infty = 11$ m/s, giving a minimum Reynolds number of $Re_\infty = U_\infty \delta / \nu = 8.8 \times 10^5$ based on an estimated full-depth boundary layer thickness of $\delta = 1.2$ m [5, 7]. Differential pressures between the upper and lower surfaces of a single square-facet heliostat were acquired simultaneously at a sampling frequency of 1 kHz using 24 high-frequency pressure sensors at the tap locations shown in Figure 2a. Each sensor has a pressure range of $\pm$ 1 psi (6.9 kPa) with an accuracy of $\pm0.2\%$ of full scale. The heliostat facet of chord length $c = 0.8$ m is attached to a circular hollow section pylon by a hinge pin joint to adjust the elevation angle α in increments of 15° between 0° and 90°, and an electronic turntable adjusts the azimuth angle β in increments of 30° between 0° and 180°. The telescopic pylon design of the heliostat (Figure 2b) allows for an adjustable elevation axis height H between 0.3 m and 0.6 m [5]. Forces on the model-scale heliostats in single and tandem (d/c from 1 to 5 with longitudinal distance d between heliostat pylons) arrangements were calculated using four $\pm$500 N three-axis load cells with an accuracy of $\pm0.5\%$ of full scale, mounted on ball joints at the corners of the force balance and turntable structure (Figure 2b, inset). To improve the accuracy of the measured forces on smaller model heliostats, a second force balance was added, equipped with three three-axis Bestech load cells, each with a capacity of ±50 N and maximum error of $\pm1.5\%$ of the measured forces. Static and dynamic wind loads on single and tandem heliostats in a range of operating and stowed configurations were investigated for a range of heliostat model sizes, with square-mirror chord lengths c from 0.1 m to 0.8 m and elevation axis heights H between 0.15 m and 0.65 m.
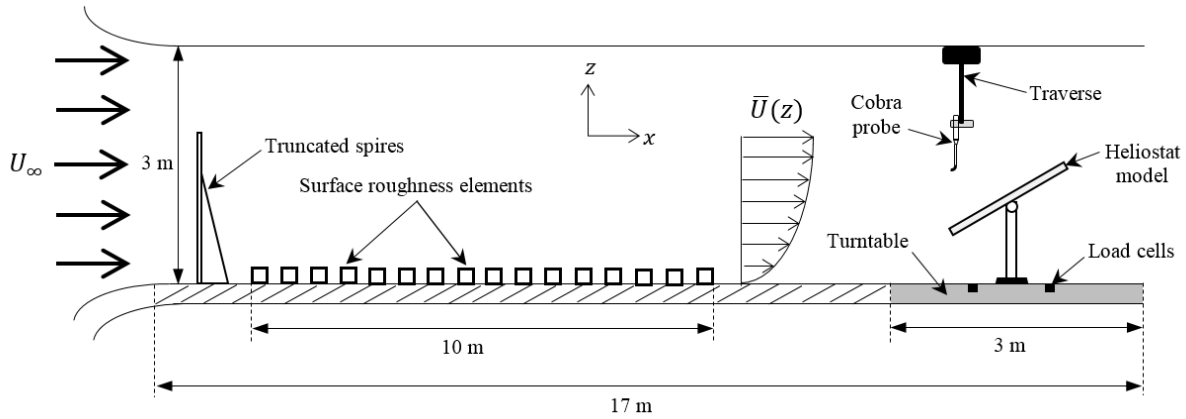
FIGURE 1. Schematic diagram of the methods used for ABL simulation and heliostat load measurements in the wind engineering test section of the University of Adelaide wind tunnel.

(a)   (b)   (c)
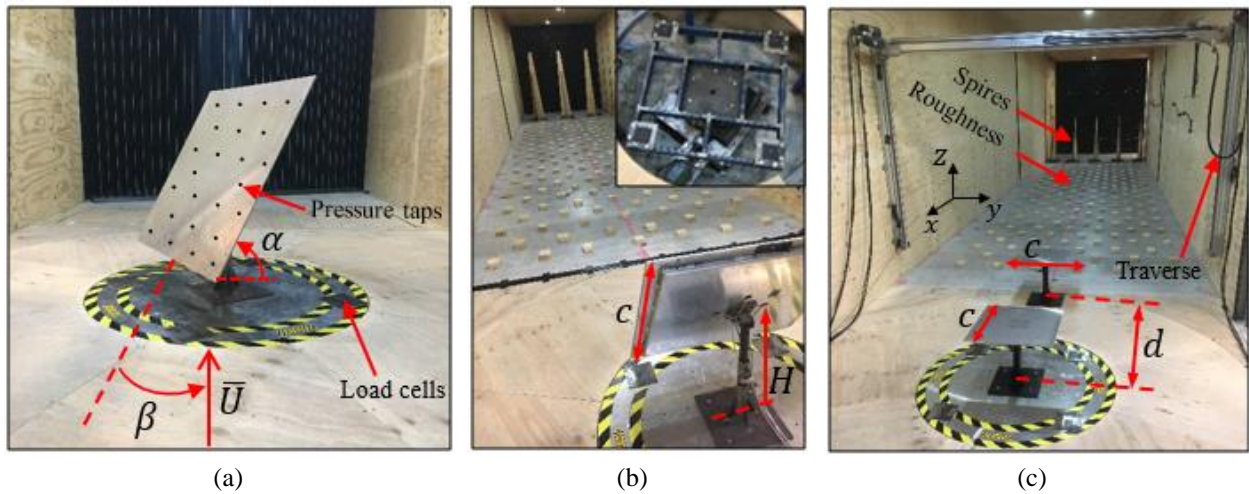
FIGURE 2. Experimental setup in the wind tunnel: (a) differential pressure tap positions on the heliostat surface at a range of elevation α and azimuth β angles; (b) load cell force measurements on a single square-mirror ($c \times c$) heliostat with adjustable pylon height H and inset, the turntable and force balance system; (c) testing of tandem heliostats and two-dimensional traverse for velocity measurements in the atmospheric boundary layer generated using spires and roughness elements.

RESULTS AND DISCUSSION

Applied Modelling Techniques in Wind Tunnel Experiments

Figure 3 presents the velocity characteristics in the longitudinal and vertical directions generated using two wind tunnel boundary layer (WTBL) arrangements of spires and roughness elements, in comparison with the theoretical logarithmic velocity profiles and ESDU 85020 [11] data of the full-scale ABL. Figure 3a shows the mean velocity profiles of WTBL1 and WTBL2 compare well with a logarithmic profile corresponding to a flat "open country" terrain ($z_0 = 0.018$ m) and a suburban terrain ($z_0 = 0.35$ m) at the range of measurement heights (0.15 m $\leq z \leq$ 0.65 m) of the heliostat models of different sizes. The turbulence intensities normalised by the local mean velocity in the longitudinal direction $I_u = \sigma_u/U$ and vertical direction $I_w = \sigma_w/U$ (Figure 3b–c) are $I_u = 13\%$ and $I_w = 9\%$ at $z = 0.3$ m in WTBL1, and $I_u = 26\%$ and $I_w = 11\%$ at $z = 0.3$ m in WTBL2. Jafari *et al.* [8] showed that the

turbulence intensities scaled to the full-scale ABL are within the allowable bandwidth of ±20% from the predicted values in ESDU 85020 [11]. However, the vertical turbulence intensity in WTBL2 is larger than ESDU estimations, which is related to the increased flow separation around the edges of the larger spires in WTBL2 generating an anisotropic, turbulent field. Figure 3d–e shows the longitudinal L_u^x and vertical turbulence length scales L_w^x in the wind tunnel boundary layers compared to the ESDU profiles. The vertical integral length scales, in general, increase with height from the ground. The longitudinal length scales are larger near the ground as the larger width of the spires generates larger turbulence structures. A similar trend is found to occur in the lowest 10-20 m of the full-scale ABL [8]. The growth of the turbulent structures in the wind tunnel is however constrained by the limited cross section of the tunnel, such that the integral length scales do not grow at the same rate as in the full-scale ABL [8]. Despite the smaller length scales that can be generated in the WTBL in comparison with the full-scale ABL, the focus of the experimental study was to determine how the size of the integral length scales relative to the heliostat chord length affect the heliostat loads.
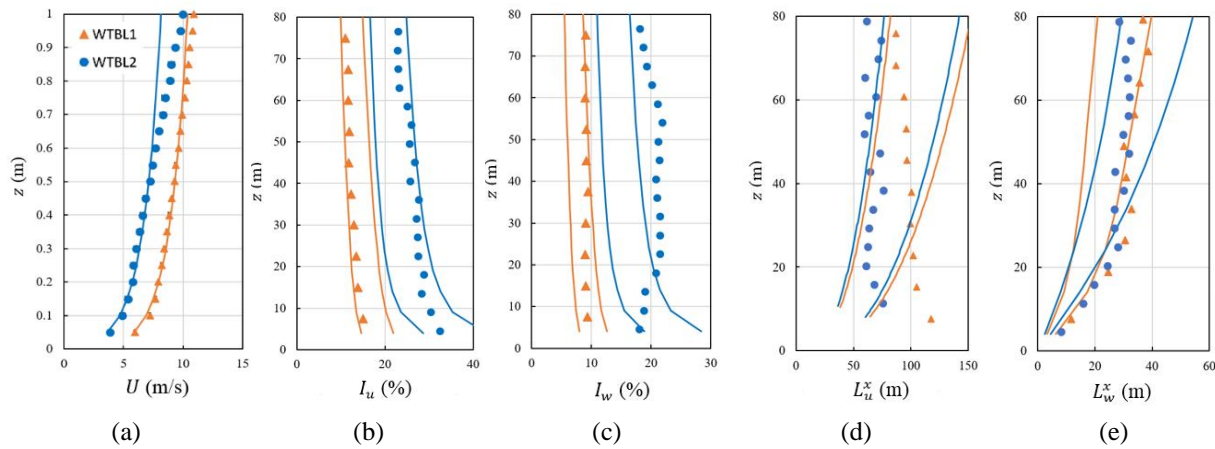
FIGURE 3. Wind characteristics of the ABLs generated in WTBL1 ($I_u = 13\%$) and WTBL2 ($I_u = 26\%$) compared to ESDU 85020 [11] data and theoretical profiles shown by the solid lines: (a) mean velocity profiles compared to logarithmic velocity profiles; (b–c) longitudinal and vertical turbulence intensity; (d–e) longitudinal and vertical turbulence length scales. The orange ($z_0 = 0.018$ m) and blue ($z_0 = 0.35$ m) lines indicate the upper and lower bounds of ±20% from the mean values of full-scale ESDU 85020 [11] data. Reproduced from Jafari *et al.* [8].

Figure 4 shows the non-dimensional form of the longitudinal (S_u) and vertical (S_w) power spectra of velocity measurements at $z = 0.3$ m in the two WTBLS, as a function of the non-dimensional frequency defined in terms of the frequency, mean wind speed U and heliostat chord length $c = 0.5$ m. The longitudinal turbulence spectra (Figure 4a) in the WTBLs follow a similar distribution to the modified form of the von Karman spectrum in ESDU 85020 [11], which indicates the similarity between the WTBLs and the lower region of the ABL. However, the peaks of the vertical turbulence spectra in Figure 4b are shifted to higher frequencies in the wind tunnel due to the different mechanism of turbulence generation in the wind tunnel, as has previously been reported in the literature [5, 12]. It must be noted that a limitation of the wind tunnel experiments on small-scale structures is that identical simulation length scale factors for the boundary layer and the heliostat model cannot be achieved. It was found that heliostat geometric scaling ratios of 1:17 and 1:24 could be used for measurement of the unsteady drag forces on the vertical heliostat, whereas measurement of the unsteady lift force on the horizontal heliostat in stow position required models to be scaled down further from full-scale by a 1:60 ratio. The differences in the turbulence spectra and aerodynamic admittance functions of these two heliostat configurations are discussed by Jafari *et al.* [13]. It is recommended that the model scale should consider the importance of matching the relevant turbulence parameters to the full-scale conditions in the reduced frequency range that contribute to the unsteady wind loads [13].
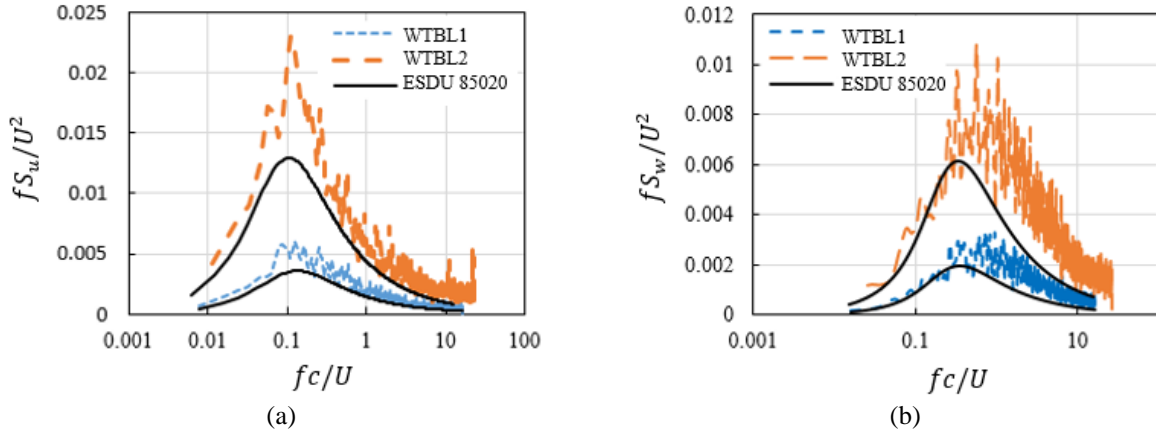
FIGURE 4. Non-dimensional power spectra based on a model heliostat ($c = 0.5$ m) at $z = 0.3$ m in the WTBLs compared to the modified von Karman form of ESDU 85020 [11]: (a) longitudinal velocity component; (b) vertical velocity component. Reproduced from Jafari *et al.* [8].

Static Wind Load on Operating and Stowed Heliostats

Figure 5 shows the peak drag and lift force coefficients on single heliostats ($\beta = 0°$) as a function of elevation angle α and turbulence intensity at the heliostat hinge height in the simulated ABLs. The peak drag force (Figure 5a) and peak lift force (Figure 5b) coefficients for operating elevation angles at $I_u = 13\%$ in the current study follow a similar trend to those of Peterka *et al.* [14] at $I_u = 14\%$. When comparing the peak load coefficients reported by Peterka *et al.* [14] at $I_u = 18\%$ with the current study at $I_u = 26\%$, the peak drag coefficient at $\alpha = 90°$ increases by 29% from 4.0 to 5.16 and the peak lift coefficient at $\alpha = 30°$ increases by 34% from 2.8 to 3.75. This confirms the approximately linear increases of the peak drag and lift coefficients on heliostats in operating [2] and stow [5, 12] positions observed with increasing turbulence at $I_u \geq 10\%$. The largest differences in the peak load coefficients between the two studies at $\alpha = 0°$ and $90°$ are likely to be caused by variations in the ratio of the turbulence length scales relative to the heliostat chord length [8, 15].
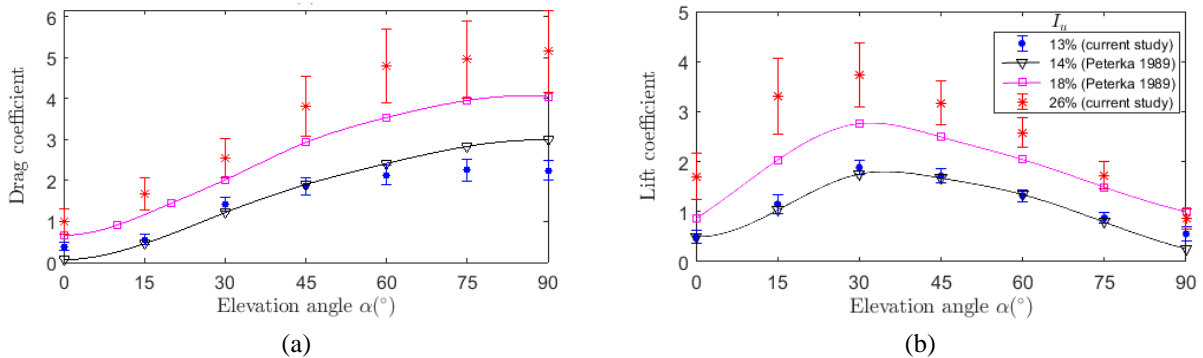
FIGURE 5. Peak aerodynamic coefficients on a single heliostat calculated as a function of longitudinal turbulence intensity I_u (%) and elevation angle and azimuth angle compared with Peterka *et al.* [14]: (a) drag force (b) lift force. Error bars represent one standard deviation of the coefficients from their mean values. Reproduced from Emes *et al.* [16].

The unsteady wind loads on stowed ($\alpha = 0°$) and vertical ($\alpha = 90°$) heliostats of different characteristic length dimensions between 0.5 m and 0.7 m were measured within WTBL1 and WTBL2 to investigate the effect of turbulence intensity and integral length scales. It was found that the peak drag force coefficient on a vertical

heliostat (Figure 6a) is well correlated with both longitudinal turbulence intensity and longitudinal integral length scale [14]. The peak lift force on the stowed heliostat (Figure 6b) was found to be mainly dependent on vertical turbulence. Hence, the peak lift coefficient is a logarithmic function of a turbulence parameter defined by vertical turbulence intensity and length scale [6].

$$\eta = I_u(L_u^x/c)^{0.48}$$

(a)

$$\eta = I_w(L_w^x/c)^{2.4}$$

(b)
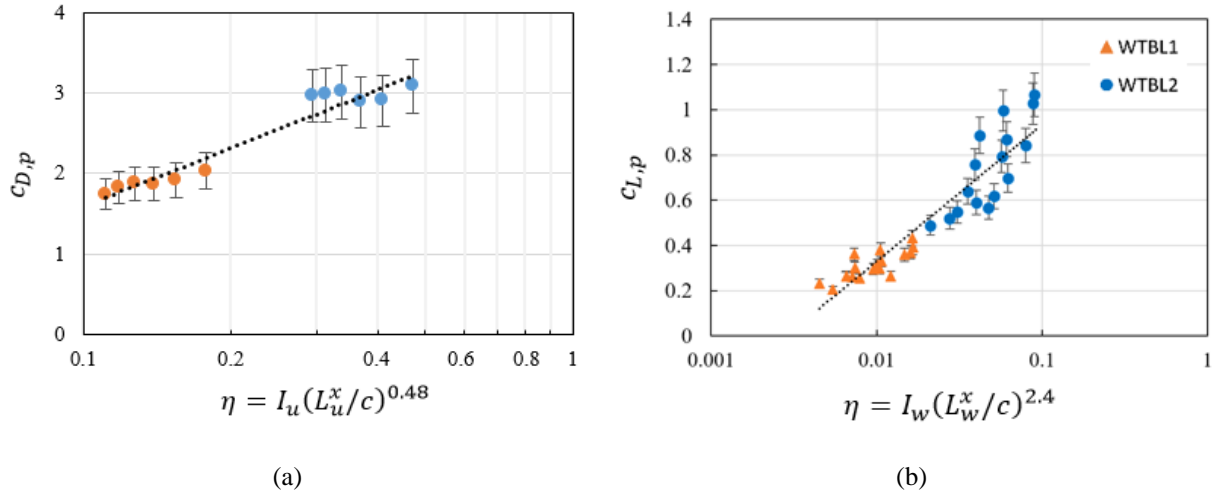
FIGURE 6. Peak aerodynamic coefficients on a single heliostat: (a) effect of longitudinal turbulence intensity and length scale on the peak drag force coefficient on a heliostat at $\alpha = 90°$; (b) effect of vertical turbulence intensity and length scale on the peak lift force coefficient on a stowed heliostat. Reproduced from Jafari *et al.* [15] and Jafari *et al.* [8].

The effect of heliostat hinge height design on the stow loads was investigated by measurement of the peak lift force for a range of H/c between 0.2 and 0.8. Figure 7 shows the normalised peak lift force coefficient on a stowed heliostat as a function of H/c for different terrain roughness values. The normalised peak lift force coefficient on stowed heliostats within the ABL is a linear function of H/c, nearly independent of the terrain roughness. This relationship indicates that decreasing H/c from 0.5 to 0.2 reduces the peak lift force coefficient on stowed heliostats by 80% for all of the terrain types. Hence, the peak lift force in stow can be reduced by up to 80% by lowering the stow height so that H/c decreases from 0.5 to 0.2 [8].
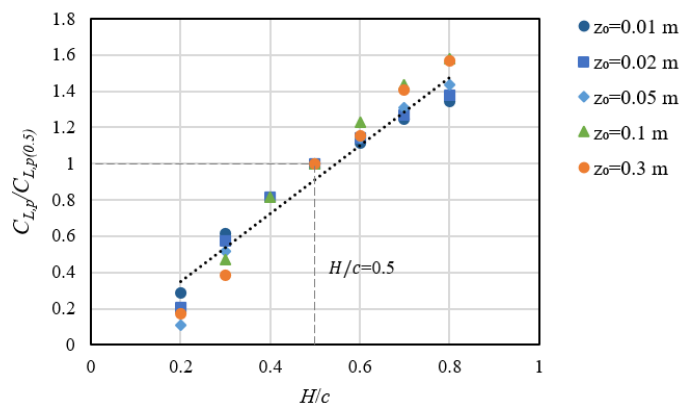
FIGURE 7. Effect of heliostat hinge-to-chord ratio H/c on the peak lift force coefficient in stow position normalised with respect to the peak lift force coefficient on a conventional azimuth-elevation heliostat with $H/c = 0.5$. The lift coefficients are presented as a function of the surface roughness length z_0 based on the turbulence parameter η defined in Figure 6b applied to full-scale ESDU 85020 [11] data. Reproduced from Jafari *et al.* [8].

Dynamic Wind Load on Single and Tandem Heliostats

Figure 8 presents the dynamic wind load characteristics of the high-frequency differential pressures between the upper and lower heliostat surfaces (Figure 2a) due to the turbulent fluctuations in the simulated ABL. The majority of the spectral energy distribution of the pressure fluctuations on a single heliostat in stow position (Figure 8a) is concentrated near the leading edge ($x = 0$ m) at frequencies below 5 Hz. In contrast in Figure 8b, the break-up of the energy-containing eddies by an upstream stowed heliostat decreased the peak spectral energy by an order of magnitude on a tandem heliostat (Figure 2c) in stow position and shifted the energy distribution to higher frequencies [6]. This shows that the upstream heliostat in stow configuration was very effective at breaking up the large energetic eddies, similar to a large-eddy break-up (LEBU) device [17]. The Strouhal number corresponding to the frequency of the largest spectral peak of the pressure fluctuations on heliostats in operating positions in Figure 8c increased by a factor of between 2 and 3 on tandem operating heliostats at $d/c = 3$ compared to those on a single operating heliostat [7]. The variation of the Strouhal number with elevation angle at each of the gap ratios d/c is similar. The increase in the fluctuating pressure frequency is therefore strongly dependent upon the existence of an upstream heliostat, but less dependent upon the positioning of the downstream heliostat. This has implications for the operating wind load design of in-field heliostats in the second row from the prevailing wind direction.


(a)   (b)   (c)
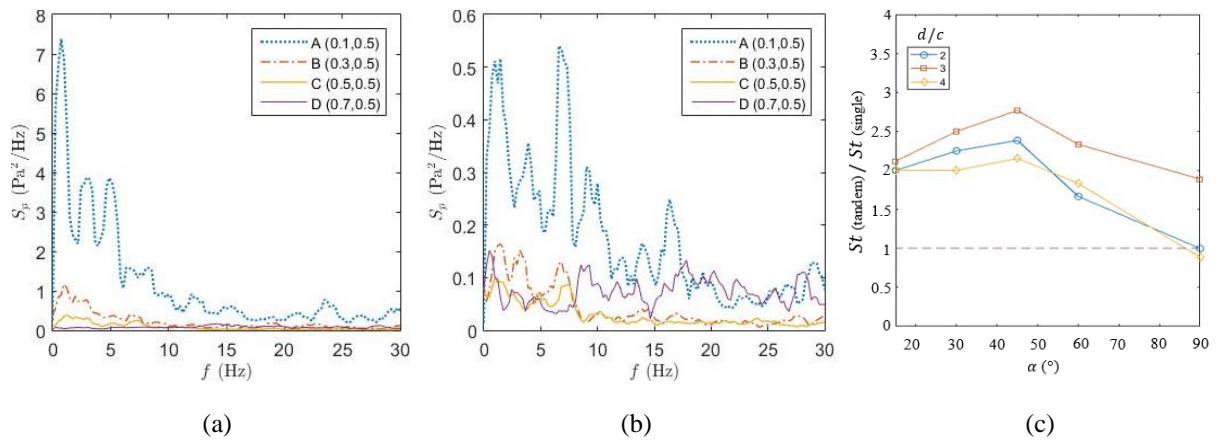
FIGURE 8. (a) Power spectral distributions of the fluctuating pressures at different positions A-D (x, y) on the surface of a single stowed heliostat with $c = 0.8$ m; (b) power spectral distributions of the fluctuating pressures at different positions A-D (x, y) on the surface of a tandem stowed heliostat ($d/c = 2$) with $c = 0.8$ m; (c) Strouhal number corresponding to the peak frequencies of the fluctuating pressure spectra on a tandem heliostat relative to a single heliostat as a function of elevation angle α and the gap ratio d/c between the tandem heliostats.

Figure 9 shows the non-dimensional peak loads on a tandem heliostat to a single heliostat as a function of the gap ratio d/c between the heliostat pylons in tandem. The peak drag force on a tandem heliostat at small elevation angles $\alpha \leq 30°$ during operation (Figure 9a) is reduced by approximately 70% relative to a single heliostat. In comparison, the drag reduction is less than 50% on tandem heliostats at $\alpha \geq 45°$. As d/c increases from 2 to 4, the non-dimensional drag force on heliostats with $\alpha \geq 45°$ approaches 1 as the two heliostats act as independent bodies. The peak drag force on a tandem normal heliostat ($\alpha = 90°$) with $d/c = 4$ increases to 10% above that on a single heliostat, whereas the normal heliostat at $d/c = 2$ has a negative drag force with approximately half of the magnitude of the single heliostat. The negative value represents a net thrust force upstream, which is significant for in-field heliostats in low-density regions at the periphery of a field during operation [7]. A different trend is observed in the variation of the non-dimensional peak lift force (Figure 9b) on a tandem heliostat in stow position relative to a single stowed heliostat. The non-dimensional lift on a tandem heliostat is up to 10% larger than a single heliostat at $d/c \leq 1$ for high-density field regions close to the tower. As d/c increases in stow position, there is a

significant decrease in the tandem lift force to maximum reductions of 20% at $d/c = 2.5$ in a moderate-turbulence ($I_u = 13\%$) ABL and 30% at $d/c = 3.5$ in a low-turbulence ($I_u = 8\%$) ABL. As d/c increases further to 5, the non-dimensional tandem lift force increases (approaching 1) more rapidly in the higher-turbulence flow due to the faster flow recovery downstream of the upstream heliostat. The results from the tandem investigations in the current study have implications for the loads on heliostats in different regions of a heliostat field. Significant reduction in the mean drag forces on operating heliostats is likely to be observed with distance into the dense region of the field close to the tower, due to the increased shielding effect of upstream heliostats with small gaps $d/c \leq 2$ between rows. However, the dynamic wind loads in these high-density regions can become significant with increased turbulence intensity induced by vortex shedding in the near wake of the upstream operating heliostats. In contrast, there is a smaller variation in the peak lift force on in-field stowed heliostats at different d/c than the drag force variation on operating heliostats. Hence, the dynamic wind loads on heliostats in stow position are most influenced by the approaching boundary layer turbulence, particularly with increasing distance from the tower at larger gaps $d/c \leq 5$ near the outer boundary of the field.
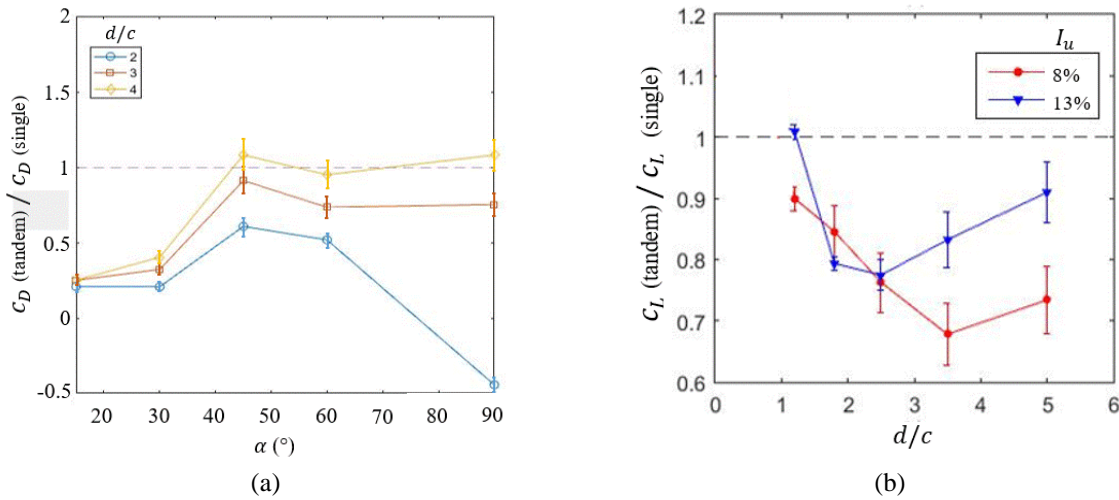
FIGURE 9. Non-dimensional peak load coefficients on a tandem heliostat relative to a single heliostat as a function of gap ratio d/c between heliostats in a tandem arrangement: (a) drag force in operating angles of elevation [7]; (b) lift force in stow position [6]. The dashed lines indicate when the load on the tandem heliostat is equal to the load on a single heliostat. The error bars represent a 10% variation of the tandem loads based on the measurement uncertainty.

The drive units and supporting pedestal-foundation of a conventional azimuth-elevation heliostat are most sensitive to the maximum wind loads, since capital cost increases at higher wind speeds due to the larger quantity of steel (per m² of surface area) required to maintain a rigid structure. Lowering of the heliostat mirror to the ground in stow position using a spindle drive [18] or a telescopic pylon [5, 8] during high-wind conditions reduces the effect of the velocity and turbulence length scales, and thus the wind load requirements and cost of the wind-bearing heliostat components. For instance, lowering the maximum operating design wind speed for stowing the heliostat from 15 m/s to 10 m/s can reduce the heliostat cost by 34% [4]. Furthermore, a 40% reduction in the peak hinge moment on the elevation drive of a conventional heliostat can lead to a 24% saving in the representative gear reducer cost [19]. The turbulence length scales that are of the same order as the heliostat characteristic length contribute most significantly to the unsteady heliostat wind loads [12, 13], and the turbulence length scales at constant height tend to increase with decreasing surface roughness of the surrounding terrain [11]. The range of cost-effective sizes of a heliostat design for minimum wind loads therefore varies depending on the site location, such as a flat desert with relatively smaller mean and gust wind speeds than in open country terrain. This area warrants further investigation to quantify the effect of gust velocities and the turbulence intensities and length scales in the lowest 10 m of the ABL on the design loads on heliostat components and hence, characterise the effect of the

surrounding surface roughness of a heliostat field site on the heliostat cost-load relationships.

Standard practice in the operation of heliostat fields is to stow the entire field during the approach of a high-wind event, such as gust front when the wind speed exceeds the threshold design wind speed. However, it is apparent that the estimated cost of the heliostat field is conservative as it adopts maximum wind load coefficients for a single heliostat, whereas the loads on heliostats in different rows presumably vary throughout the field. As an example, during operation of a surround field of 500 m radius containing 35,000 heliostats, the elevation angle of the heliostats located at the edge of the 150 MW field vary between 13° and 77° [20]. Furthermore, the elevation angles of two heliostats positioned at radial distances R of 100 m and 362 m from a 100-m tower can differ by up to 15° when tracking throughout a day [21]. For an assumed constant maximum operating design wind speed that would nominally stow the entire field to reduce the maximum hinge moment on the elevation drive at $\alpha \approx 30°$, the majority of the heliostats in the outer region of the field ($R = 362$ m) with $\alpha = 25\text{-}40°$ [21] would need to be stowed but the in-field heliostats ($R = 100$ m) close to the tower with $\alpha = 40\text{-}55°$ [21] could continue to operate throughout this period. Hence, there is a significant potential at some sites to reduce the maximum operating design wind speed and thus the cost by designing the inner circle of heliostats to be lighter [4]. Development of a smart-control stow strategy for protecting only the outer exposed region of a field during high-wind events has the potential to yield additional operating hours of the heliostat field throughout a day over a larger range of wind speeds without compromising the strength and mass of material in the heliostat design. Alternatively, the positioning of low-cost slender plate structures aligned horizontally (analogous to a heliostat in stow position) at the outer exposed boundary of a heliostat field can effectively act as a large-eddy break-up (LEBU) device that attenuates the energy of the velocity fluctuations and reduces the turbulence length scales of the flow approaching the in-field heliostats during operation of the plant.

CONCLUSIONS

This study summarised the extensive high-fidelity wind tunnel experiments in the Heliostat Wind Load Project within the Australian Solar Thermal Research Institute (ASTRI). Applied modelling techniques using a range of truncated spires and roughness elements were adopted for generation and characterisation of the temporal and spatial turbulent fluctuations in the lower region of the atmospheric boundary layer (ABL) where full-scale heliostats are positioned. Heliostat wind loads were found to be highly dependent on the critical scaling parameters of the heliostat and the energetic eddies in the turbulent flow. The following conclusions can be drawn from the experimental investigations in the current study:

- Loads on heliostats at elevation angles approaching a normal position during operation were largely influenced by the longitudinal turbulence components in the ABL, whereas the loads on heliostats in stow position were closely correlated to the vertical turbulence intensity and length scales.
- A telescopic pylon in the heliostat design revealed that the peak lift force in stow position could be reduced by up to 80% by lowering the stow height from 50% of the heliostat chord length to 20% of the heliostat chord length.
- The peak quasi-static loads on tandem heliostats in stow and operating positions were reduced by 30-50% relative to those on a single heliostat.
- The dynamic loads associated with the peak spectral energy of the fluctuating pressures on the heliostat surface were reduced by a factor of three on tandem heliostats in operating positions relative to a single heliostat at the same elevation angle and by an order of magnitude on a tandem heliostat in stow configuration relative to a single stowed heliostat.

The results in this work can be used to determine heliostat configurations and appropriate design wind speeds in different terrains leading to the maximum design wind loads on the wind-bearing heliostat drives and foundation. The objectives of future work in ASTRI are to develop wind load design guidelines for the scaling relationships between heliostat wind loads and ABL turbulence based on wind tunnel and field experiment data.

ACKNOWLEDGMENTS

REFERENCES

1. J. A. Peterka and R. G. Derickson, *Wind load design methods for ground-based heliostats and parabolic dish collectors* (Sandia National Laboratories, Albuquerque, New Mexico, 1992), SAND92-7009.
2. J. A. Peterka, Z. Tan, B. Bienkiewicz and J. Cermak, *Wind loads on heliostats and parabolic dish collectors: Final subcontractor report* (Solar Energy Research Institute, Golden, Colorado, 1988), SERI/STR-253-3431.
3. G. J. Kolb, C. K. Ho, T. R. Mancini and J. A. Gary, *Power tower technology roadmap and cost reduction plan* (Sandia National Laboratories, Albuquerque, 2011), SAND2011-2419.
4. M. J. Emes, M. Arjomandi and G. J. Nathan, Effect of heliostat design wind speed on the levelised cost of electricity from concentrating solar thermal power tower plants, Solar Energy **115**, 441-451 (2015).
5. M. J. Emes, M. Arjomandi, F. Ghanadi and R. M. Kelso, Effect of turbulence characteristics in the atmospheric surface layer on the peak wind loads on heliostats in stow position, Solar Energy **157**, 284-297 (2017).
6. M. J. Emes, F. Ghanadi, M. Arjomandi and R. M. Kelso, Investigation of peak wind loads on tandem heliostats in stow position, Renewable Energy **121**, 548-558 (2018).
7. J. S. Yu, M. J. Emes, F. Ghanadi, M. Arjomandi and R. M. Kelso, Experimental investigation of peak wind loads on tandem operating heliostats within an atmospheric boundary layer, Solar Energy **183**, 248-259 (2019).
8. A. Jafari, F. Ghanadi, M. Arjomandi, M. J. Emes and B. S. Cazzolato, Correlating turbulence intensity and length scale with the unsteady lift force on flat plates in an atmospheric boundary layer flow, Journal of Wind Engineering and Industrial Aerodynamics **189**, 218-230 (2019a).
9. M. J. Emes, A. Jafari, F. Ghanadi and M. Arjomandi, "A method for the calculation of the design wind loads on heliostats," in *SolarPACES*, (AIP Conference Proceedings, Casablanca, Morocco, 2019a).
10. H. Irwin, The design of spires for wind simulation, Journal of Wind Engineering and Industrial Aerodynamics **7**, 361-366 (1981).
11. ESDU 85020, *Characteristics of atmospheric turbulence near the ground, Part II: single point data for strong winds (neutral atmosphere)*, Engineering Sciences Data Unit, London, 2001, ESDU 85020.
12. A. Pfahl, M. Randt, F. Meier, M. Zaschke, C. Geurts and M. Buselmeier, A holistic approach for low cost heliostat fields, Energy Procedia **69**, 178-187 (2015).
13. A. Jafari, F. Ghanadi, M. J. Emes, M. Arjomandi and B. S. Cazzolato, Measurement of unsteady wind loads in a wind tunnel: scaling of turbulence spectra, Journal of Wind Engineering and Industrial Aerodynamics **193**, 103955 (2019b).
14. J. A. Peterka, Z. Tan, J. E. Cermak and B. Bienkiewicz, Mean and peak wind loads on heliostats, Journal of Solar Energy Engineering **111**, 158-164 (1989).
15. A. Jafari, F. Ghanadi, M. J. Emes, M. Arjomandi and B. S. Cazzolato, "Effect of Free-stream Turbulence on the Drag Force on a Flat Plate," in *AFMC*, Adelaide, Australia, 2018).
16. M. J. Emes, A. Jafari, F. Ghanadi and M. Arjomandi, Hinge and overturning moments due to unsteady heliostat pressure distributions in a turbulent atmospheric boundary layer, Solar Energy **193**, 604-617 (2019b).
17. C. Chin, R. Örlü, J. Monty, N. Hutchins, A. Ooi and P. Schlatter, Simulation of a large-eddy-break-up device (LEBU) in a moderate Reynolds number turbulent boundary layer, Flow, Turbulence and Combustion **98**, 445-460 (2017).
18. A. Pfahl, F. Gross, P. Liedke, J. Hertel, J. Rheinländer, S. Mehta, J. F. Vásquez-Arango, S. Giuliano and R. Buck, "Reduced to Minimum Cost: Lay-Down Heliostat with Monolithic Mirror-Panel and Closed Loop Control," in *SolarPACES 2017*, (AIP Conference Proceedings 2033, Santiago, 2017b).
19. K. Lovegrove and W. Stein, Concentrating solar power technology: principles, developments and applications, Woodhead Publishing Limited, Cambridge, UK, 2012.
20. J. Vásquez-Arango, Dynamic Wind Loads on Heliostats, PhD Thesis, DLR, Uni Aachen, 2016.
21. A. Zeghoudi and A. Chermitti, Estimation of the Solar Power Tower Heliostat Position using Neural Network, International Journal of Computer Applications **94**, 41-46 (2014).